Editor summary:

A review of NIR-II fluorescence imaging is presented, with a focus on fluorophores and probes and imaging techniques.

Reviewer Recognition:

Nature Photonics thanks Jun Qian and the other, anonymous, reviewer(s) for their contribution to the peer review of this work.

In vivo NIR-II fluorescence imaging for biology and medicine

Feifei Wang[1], Yeteng Zhong[2], Oliver Bruns[3,4], Yongye Liang[5], Hongjie Dai[6,7]*

[1]Department of Electrical and Electronic Engineering, The University of Hong Kong, Hong Kong 999077, China

[2]CAS Key Laboratory for Biomedical Effects of Nanomaterials and Nanosafety, CAS Center for Excellence in Nanoscience, National Center for Nanoscience and Technology, Chinese Academy of Sciences, Beijing100190, China

[3]Department for Functional Imaging in Surgical Oncology, National Center for Tumor Diseases (NCT/UCC) Dresden, Germany

[4]Helmholtz Pioneer Campus, Helmholtz Zentrum München, Neuherberg, Germany

[5]Department of Materials Science and Engineering, South University of Science and Technology of China, Shenzhen, China.

[6]Department of Chemistry and Bio-X, Stanford University, Stanford, CA 94305, USA

[7]Department of Chemistry, School of Engineering and School of Biomedical Sciences, The University of Hong Kong, Hong Kong 999077, China

* Correspondence to: hdai@stanford.edu

Abstract

Due to reduced light scattering and tissue autofluorescence, in vivo fluorescence imaging in the 1000 - 3000 nm near-infrared II (NIR-II) spectral range can afford non-invasive imaging at millimetres-depths within biological tissue. Infrared fluorescent probes labelled with antibodies or other targeting ligands also enable NIR-II molecular imaging at the single cell level. In this Review, we present recent developments in the design of fluorophores and probes emitting in the NIR-II window based on organic synthesis and nanoscience approaches. We also review advances in NIR-II wide-field and microscopy imaging modalities, with a focus on

preclinical imaging and promising clinical translation case studies. Finally, we outline current issues and challenges for the wider adoption of NIR-II imaging in biomedical research and clinical imaging.

1. Introduction

Optical imaging is important to biology and medicine as it boasts exceptional spatiotemporal resolution for non-invasive in vivo imaging with potentially diffraction limited or sub-diffraction limited spatial resolution in real time, which complements X-ray computed tomography, magnetic resonance imaging and ultrasound imaging. However, the spatial resolution and penetration depth of in vivo fluorescence imaging into live tissues is limited by combined effects of absorption, scattering, tissue autofluorescence, quantum yields (QY) of probes, optical configuration and detector sensitivity/efficiency. High resolution fluorescence imaging relies on ballistic and slightly scattered snake-like photons transmitting through tissues, whereas multiple-scattered diffusive photons contribute to noise or background and ruin the diffraction-limited resolution [1,2]. Light scattering within tissues is dominated by Rayleigh and Mie scattering [3], both decreasing as $\lambda^{-\alpha}$ at longer wavelengths [4] (Fig. 1a), where λ is imaging wavelength and α = 0.2-4 for tissues [5]. Reduced light scattering can afford deeper and higher-contrast fluorescence imaging with less diffusive noise at longer wavelengths.

For decades near-infrared imaging in the 700-900 nm NIR-I window has been pursued for in vivo biomedical imaging [6] to benefit from suppressed light scattering by tissues compared to visible light as well as lower absorption by hemoglobin [7]. NIR-I fluorescence imaging became widely accepted owing to successes of fluorophores such as indocyanine green (ICG), and the advent of digital imaging technology in the early 2000s [8]. However, in vivo imaging in NIR-I still suffers from light scattering caused feature blurring, shallow penetration depth and high background due to both scattering and autofluorescence from endogenous chromophores or pigmented components in the body [9,10].

The Dai group in 2009 demonstrated the first 1000-1700-nm NIR-II preclinical fluorescence imaging of mice using hydrophilic polymer coated single-walled carbon nanotubes (SWNTs) and a liquid nitrogen cooled indium gallium arsenide (InGaAs) camera [11]. In 2022, the group performed in vivo imaging in the 1700-2000 nm range and refined the definition of NIR-II to be 1000-3000 nm [12], largely overlapping with the 900-3000 nm short-wave infrared (SWIR) range. Subsequently the group established NIR-II superior spatial resolution, imaging depth, signal/background ratio (SBR) and diminished tissue autofluorescence over NIR-I imaging [5,10-29]. Light absorption by water in biological tissues and light scattering by tissues limit light penetration depth into a living body. Considering water absorption by vibrational overtone modes, tissue scattering of light, and the detection range of ~900-1700 nm of InGaAs cameras, one can divide the NIR-II range into several sub-windows with local maxima in light penetration depth vs. wavelength (Fig.1b) [12], including NIR-IIa (1300-1400 nm), NIR-IIb (1500-1700 nm), NIR-IIc (1700-2000 nm) and NIR-IId window (~2100–2300 nm). Moderate light absorption of water in the 1400-1500 nm range was shown to enhance NIR-II image contrast due to multiply scattered diffusive light decays faster than ballistic light [30,31]. Beyond NIR-IId light absorption by vibrational normal modes of water is

too overwhelming, making through-tissue fluorescence imaging impossible [12]. Fluorescence imaging of a fluorophore-filled capillary through different thicknesses of tissue phantoms made of intralipid solutions (Fig. 1c) [12] and mouse brain (Fig.1d) [17] showed clearly improved resolution and SBR when transitioning from NIR-I, IIa to IIb and IIc sub-windows. This is because high resolution and low feature smearing hinge on low scattering, afforded with longer wavelength light. NIR-II imaging beyond 1 cm tissue depth has been demonstrated [32].

Notably, although NIR-I light exhibited much lower light absorption, tissue penetration depth is much shallower than NIR-II light due to scattering (Fig. 1b), making NIR-II imaging a step-out technology over the traditional NIR technique. Large Stoke's shift between excitation (typically 808 nm) and emission for wide-field imaging in the > 1500 nm NIR-IIb, IIc and IId sub-windows eliminates any tissue autofluorescence background (Fig. 1d) even in mouse liver [10]. NIR-IIb and IIc regions are the highest performing sub-windows for in vivo NIR-II imaging.

2. Recent progress in NIR-II fluorophores and nanoprobes

Fluorescent probes for biological imaging should exhibit high brightness (high QY and molar absorptivity/extinction coefficient) and biocompatibility. The QY of NIR-II fluorophores is lower than visible or NIR-I counter-parts. In molecular fluorophores, non-radiative relaxation between the zero-vibrational level of excited states and the higher isoenergetic vibrational levels of the ground state can quench the molecular fluorescence [33]; and this effect, called the 'energy gap law', becomes more pronounced as the energy gap shrinks at longer wavelengths. In aqueous environments, the NIR-II molecular fluorophores, typically with larger π-conjugated backbones, suffer from stronger intermolecular interactions, which lead to further non-radiative decay of the NIR-II emission [34]. The abundance of hydroxyl groups in aqueous solution is also reported to be a serious quencher to NIR-II luminescence of rare-earth nanoparticles (RENPs) [19]. The nonpolar conjugated backbones of molecular fluorophores and the hydrophobic capping layers of inorganic nanoparticles require effective hydrophilic modification for biocompatibility, a process that decreases the fluorescence QY drastically. Despite these challenges recent years have witnessed an outpouring of promising high-performance NIR-II probes.

Inorganic nanostructured NIR-II probes. The first NIR-II imaging [11] utilized SWNTs photoluminescent in the 1000-1700 nm range (Fig. 2a) [13] depending on nanotube chirality and diameter in the 0.7-1.4 nm (Fig. 2b) [5,15,17,35]. NIR-II quantum dots (QDs) included silver sulfide (Ag_2S; 1100-1400 nm) [16,36], lead sulfide (PbS; 1000-2000 nm; QDb: 1500-1700 nm and QDc: 1700-2000 nm; Fig. 2c) [12,21], and indium arsenide (InAs; 900-1600 nm) [37], exhibiting higher fluorescence QY than SWNTs. These QDs were typically overcoated with a passivation shell to avoid oxidation and afford core-shell QDs with bright NIR-II emission in aqueous solutions [25,33,40]. Down-conversion RENPs showed fascinating optical properties such as narrow-band emission spanning NIR-II range [38], long luminescence lifetime (up to 10's of ms scale) [39], and Auger effect based persistent luminescence after X-ray irradiation [40]. To enhance NIR-II emission, we developed Ce^{3+}-doping [19] and cubic-phase [23] strategies to suppress up-conversion while boosting Er^{3+} down-conversion luminescence at 1550 nm by ~ 9-fold and ~ 8-fold,

respectively. More recently, cubic-phase RENPs based on Tm^{3+} emitter were developed (Fig. 2e), exhibiting 1600-1700 nm sub-NIR-IIb fluorescence amplification [41]. Finally, gold molecular clusters with ultra-small size (Au_{25} ~1.6 nm, Fig. 2f) exhibited luminescence in 1000-1400 nm [27,42,43].

Inorganic nanostructured NIR-II probes are often synthesized in organic solvents. To impart biocompatibility for preclinical use, we coated the probes with three hydrophilic, cross-linked polymer layers ('P^3 coating'; Fig. 2g) to impart high biocompatibility [23,25]. The P^3 cross-linked surface coating enabled rapid biliary clearance and reduced the long-term retention induced side effects of a wide range of nanomaterials, including RENPs, PbS QDs, and superparamagnetic iron oxide nanoparticles, enhancing their in vivo pharmacokinetics and the potential use for nanomedicine [25].

Molecular fluorophores. Molecular fluorophores are important NIR-II probes due to well-defined structures, rich chemical and structural tunability, and generally high biocompatibility and favorable pharmacokinetics. Thus far, NIR-II molecular fluorophores include polymethine (Fig. 2h) [44,45], donor-acceptor molecules (Fig. 2i) [18,46,47], boron-dipyrromethene (BODIPY, Fig. 2j) [48], rhodamine (Fig. 2k) [49] and metal-macrocycles complexes (Fig. 2l) [50]. High performance in vivo NIR-II fluorescence imaging have been demonstrated using organic fluorophores exhibiting advanced properties such as long wavelength peak absorption up to 1400 nm [45], large absorption coefficient of 10^5 $mol^{-1} \cdot cm^{-1}$ [51], high quantum yields (QY) of > 5% [47], or long emission in the NIR-IIb window [52]. These molecules generally have large conjugated backbones with high hydrophobicity. For aqueous solubility researchers typically encapsulate the molecules in amphiphilic polymer matrixes [21,53] or functionalize them with hydrophilic side chains [54].

The absorption/emission wavelength of NIR-II molecular fluorophores can be red-shifted by increasing the conjugated backbone length [52], increasing donor/acceptor unit strength [55], or forming J-aggregates [45]. Video-rate multicolor imaging with NIR-II fluorescence under multiplexed excitation wavelength has been demonstrated with flavylium polymethine dyes with finely tuned heterocycle modification [44]. Due to the energy gap law, red-shifted fluorophores generally show lower QY, especially for molecular fluorophores with peak absorption over 1000 nm. Strong interactions between water molecules and conjugated backbones cause substantial non-radiative decay for NIR-II molecular fluorophores [54,55], Protecting the conjugated backbones from water molecules is vital for high fluorescent QY in aqueous conditions.

An advantage of organic NIR-II fluorophores over inorganic nanoparticle probes is the smaller sizes that favor renal excretion upon administration to a body. Renal excretion of NIR-II probes is preferred for potential clinical use since excretion through the kidney/urinary pathway is fast, making them safer and less likely to cause toxic effects than probes remaining in the body for extended times. To date, only several NIR-II molecular fluorophores have been reported with renal-excretion ability [18,20,48,56]. A caveat is that attaching highly hydrophilic side groups such as β-cyclodextrin (β-CD) [56] and poly(oligo(ethylene glycol) dimethacrylate) polymer brushes [48] to NIR-II fluorophores can facilitate renal excretion, but typically lowers

the fluorescence QY due to non-radiative relaxation of excited states by strong fluorophore-water interactions.

Fluorescent proteins. Genetically encoded fluorescent proteins (FPs) have been widely deployed for long-term visualizing and tracking of molecules, cells or structures with high specificity in cells or organisms. Recently, towards NIR-II imaging of FPs for reduced light scattering, improved imaging depth/resolution and reduced diffused noise [57], there has been a growing interest in the emission tails of NIR-I FPs into the > 1000 nm NIR-II window. Bacterial phytochrome photoreceptors (BphPs), cyanobacteriochromes (CBCRs) and allophycocyanins (APCs) have been employed as a source to design NIR-I FPs [58]. It has been demonstrated that FPs engineered from BphPs (e.g. iRFP670, iRFP682, iRFP702, iRFP713, and iRFP720) [59] and CBCRs (e.g. monomeric miRFP670nano and miRFP718nano) [60] exhibit fluorescence emission tails in the NIR-II window. iRFP713 has been knocked into the mouse genome for long-term monitoring of liver regeneration models and imaged at > 900 nm [59]. The NIR-II fluorescence of miRFP718nano was three times brighter than miRFP670nano and 1.5- and 2-times brighter than that of miRFP709 and miRFP703, respectively [60]. The performance of miRFP718nano was evaluated for liver inflammation models beyond 1050 nm, using 50 $mWcm^{-2}$ excitation and a 30 ms exposure time [60].

3. NIR-II imaging modalities

NIR-II 2D wide-field imaging. NIR-II wide-field fluorescence imaging employs an excitation source such as expanded laser beam [11], light-emitting diode (LED) [23], X-ray beam [61] or Cerenkov radiation [62] (Fig. 3a) to illuminate an entire 3D object (e.g., a mouse) and projects the generated NIR-II fluorescence to a 2D image captured by a camera . Non-coaxial excitation is commonly employed to avoid the use of dichroic mirrors and background signals due to intense reflections from the samples. Other NIR-II wide-field modes requires no excitation source, including chemiluminescence [63], bioluminescence [64] and afterglow fluorescence imaging [40]. Wide-field imaging of phantoms or tissues showed penetration depth and resolution of NIR-II imaging are ~ 1.7 [5,17,32,59,64-66] and ~ 2.1 [15,17,66-69] times better than NIR-I imaging, respectively, but significantly influenced by the imaging conditions.

NIR-II imaging in various sub-windows employs a suitable camera and optical filters on the camera side. For NIR-IIa and NIR-IIb fluorescence imaging, a cooled InGaAs camera (900-1700 nm) with wide dynamic range and low read noise and dark current is used. For NIR-IIc and NIR-IId wide-field imaging, cameras based on photosensitive semiconductors with small bandgaps, such as “extended InGaAs” (900-2600 nm), indium antimonide (InSb, 960-5000 nm) and mercury cadmium telluride (HgCdTe or MCT, 800-14000 nm) are required. Recently, NIR-IIc wide-field imaging was explored utilizing a MCT camera [70], but with the caveat of higher-cost, higher noise and lower sensitivity than commonly used InGaAs cameras. NIR-II imaging acquisition speed has reached to 300 fps using a fast InGaAs camera [71]. The resolution of NIR-II wide-field imaging with a field-of-view (FOV) covering the entire mouse is ~ 100 μm limited by the small numbers of pixels of available cameras.

For NIR-II imaging-guided surgery, a multispectral system is essential, allowing concurrent visible photographic and NIR-II fluorescence/luminescence imaging under bright surgical

room-light conditions (Fig. 3a). To avoid imaging parallax, color camera and NIR-II camera could share the same chromatic aberration corrected lens set [28] or use two separate lens sets sharing a portion of the same coaxial optical path [72], allowing both cameras to capture the same location from the same angle.

NIR-II 3D confocal microscopy. A NIR-II confocal microscope employs a laser beam tightly focused to a point raster scanned in *x-y-z* to excite fluorophores point-by-point in a sample. At each point the emitted fluorescence was detected after passing through a pinhole to reject out-of-focus signals, and signal is used for constructing a 3D image (Fig. 3b). Confocal NIR-II fluorescence imaging increased the tissue penetration depth limit by ~ 10 fold over visible confocal microscopy (< 100 μm in visible). The penetration depth of confocal microscopy can be optimized by employing both long excitation and emission wavelengths, high quantum yield fluorophores and detectors with high sensitivity and low noise.

Initially NIR-II confocal microscopy was realized by using NIR-I excitation, NIR-II emission and an InGaAs photomultiplier tube (PMT) detector [21,73]. For examples, NIR-IIb confocal imaging of QDb in mouse blood vasculatures under a 785-nm excitation resolved blood vessels at ~ 700 μm in intact tumors on mice with sub-10 μm resolution [21]. Confocal imaging of aggregation-induced emission (AIE) dots filled cerebral blood vessels after craniotomy was performed using 793 nm excitation and > 1000 nm emission, achieving 800 μm penetration depth in mouse brain with ~ 9 μm resolution [74]. Recently we exploited superconducting nanowire single-photon detector (SNSPD) for NIR-II confocal microscopy and found it superior to InGaAs PMT with shorter timing jitter, higher sensitivity, and lower noise [12]. A home-built SNSPD with a timing jitter of ~ 109 ps was demonstrated to realize NIR-II lifetime imaging using an 800-nm femtosecond laser for excitation [75].

NIR-II confocal microscopy with 1310 nm excitation, QDb probes and a SNSPD enabled cerebral blood vessels imaging in vivo at a depth of ~ 1.7 mm into the hippocampus region after craniotomy [76], close to the ~ 1.6 mm imaging depth achieved by 1280-nm excited two-photon microscopy [77]. The tunable spectrum-response range of SNSPD presents opportunities for confocal imaging in the NIR-IIc and NIR-IId windows beyond the detection limit of InGaAs PMT. To push the penetration depth limit of in vivo non-invasive one-photon imaging, NIR-IIc confocal microscopy with 1650-nm excitation was demonstrated using QDc and a SNSPD, reaching an imaging depth of ~1.1 mm into an intact mouse head. It also allowed non-invasive through tissue molecular imaging of mouse inguinal lymph nodes with single-cell and single-vessel resolution (Fig. 3b, middle and right) [12]. This was the first time that both excitation and emitted light in the > 1500 nm regime were utilized for in vivo confocal imaging to minimize light scattering and maximize imaging depth.

The longest excitation wavelength of 1650 nm for NIR-II one-photon confocal microscopy is close to that (~1700 nm) used by multi-photon microscopy [78], with the excitation light intensity decaying similarly traversing through tissues. The one-photon fluorescence emission of the excited probes scales linearly with excitation light intensity, while two-photon and three-photon fluorescence scale with the second and third power of the excitation, respectively [12,79]. This suggests slower emission intensity decay and deeper imaging depth of confocal microscopy than multi-photon microcopy with similar excitation wavelength. In vivo NIR-IIc

confocal microscopy can be done non-invasively through intact tissues, in contrast to multiphoton intravital microscopy. Multi-photon imaging is advantageous in higher SBR [79] and the availability of genetically engineered probes. By combining NIR-IIc confocal microscopy with multiphoton microscopy that both uses ~1650-1700 nm excitation, one could maximize the capability of multichannel molecular-specific and cellular-specific imaging to investigate complex biological systems in vivo.

NIR-II 3D light sheet microscopy. Light sheet microscopy (LSM) utilizes orthogonally arranged illumination and wide-field detection to afford high-speed optical sectioning and three-dimensional volumetric imaging, an approach capable of minimal phototoxicity and subcellular resolution [80] or sub-diffraction limited resolution by using lattice illumination and adaptive optics [81]. However, the imaging depth of LSM for in vivo imaging of live tissues in the visible window is shallow, ~ 200 μm for mouse brain after craniotomy [24] due to light scattering. Two-photon light sheet microscopy at 1040 nm allows for deeper imaging into mouse brain (up to ~ 300 μm) with high resolution owning to reduced scattering of the NIR-II excitation [82]. The penetration depth can be further extended by using Bessel [83] or Airy beam [84] for excitation, but it is still limited by scattering of the visible emitted light.

An oblique NIR-IIb LSM with ~ 1319 nm excitation and ~ 1500-1700 nm detection was developed for in vivo mice imaging with cellular resolution [24] (Fig. 3c, middle). NIR-II LSM prevented shadows and stripes caused by tissue scattering and absorption, problems common to visible LSM. NIR-IIb LSM enabled non-invasive imaging/sectioning of intact mouse head with a total penetration depth of ~ 750 μm, resolving vascular channels connecting the skull and brain cortex of mice. These channels were used by immune cells trafficking between the skull bone marrow and cortex for immune protection of mouse brain [85]. In another application, PD-1$^+$ cells migrating irregularly in tumor vasculatures were monitored by NIR-IIb LSM at a frame rate of 20 fps (Fig. 3c, bottom left).

The wavelength of NIR-II light is two to four times longer than visible light; the diffraction-limited spatial resolution (Rayleigh criteria [86], 0.61λ/NA) of NIR-II LSM is lower than visible LSM. In addition, NIR-II imaging at deep tissues still experienced light scattering, causing background increase and reduced spatial resolution. A scanning Airy beam with self-healing or attenuation-compensation properties [84] was employed for excitation [87] in NIR-II LSM to improve SBR, tissue penetration and *z*-direction resolution.

Structured illumination has been introduced into NIR-II LSM to improve spatial resolution by extracting high-frequency details embedded in low-resolution moiré fringes [88] imaged under a scanning Gaussian-beam comb pattern with several shifted phases [26]. The NIR-II structured-illumination LSM can minimize background interference, increase SBR and increase spatial resolution by up to 2 times [26] (Fig. 3c, right), and has been utilized for longitudinally imaging of immune cells in response to immunotherapy in the tumor microenvironment of a mouse model [26]. The resolution can be further enhanced by using objectives with a higher NA.

4. Applications in preclinical imaging

NIR-II imaging has been extensively performed preclinically since 2009 for (1) visualizing blood vasculature structures, measuring hemodynamics and perfusion for cardiovascular diseases; (2) lymph node imaging; (3) molecular imaging and (4) functional imaging.

Vascular and hemodynamic imaging. Dynamic NIR-II imaging speed for hemodynamics increased from the initial ~ 5 fps using SWNT probes [89] to recently ~ 90 fps using ErNPs [23]. Cardiovascular disease models have been investigated by NIR-II imaging using circulating carbon nanotubes [5], QDs [37], AIE nanodots [90] and gold clusters [91] respectively. Dynamic monitoring of blood perfusion and hemodynamics in individual blood vessels for disease models of peripheral arterial disease (PAD) [15,89], middle cerebral artery occlusion (MCAO) stroke [5] (Fig. 4a), and traumatic brain injury (TBI) [92] were performed. Vascular regeneration was imaged with PbS/CdS QDs in the NIR-IIb window longitudinally in a mouse model of PAD. Blood flow was also imaged with InAs QDs in disordered vasculatures in glioblastoma multiforme tumor to observe the impact of brain tumor growth on cerebral vasculatures (Fig. 4b)[37]. The tumor, arterial vessels and venous vessels were identified by dynamic contrast-enhanced imaging through principal component analysis (PCA) [6,18,23,25,40].

Lymph node imaging. Sentinel lymph nodes (LNs) are the initial drainage nodes of the primary tumor where cancer metastasis first occurs. Locating the sentinel LNs for biopsy is important to assessing metastatic spread to the LN basin [93]. NIR-II fluorescence imaging provides accurate localization of LNs and lymphatic vessels with better contrast and resolution than in the NIR-I window [25,94,95]. Recently 'super-stealth' Au-phosphorylcholine (Au-PC) nanocluster probes were developed for imaging the draining LNs of cancer tumors after intratumoral administration, with minimal interference by surrounding tissues in vivo (Fig. 4c) [27].

Molecular Imaging. NIR-II molecular imaging of tumor biomarkers have been pursued with t
argeted NIR-II probes conjugated with antibodies or other ligands, capable of high spatial r
e
s
o
l
u
t
i
o
n

High endothelial venules (HEVs) in LNs are small postcapillary venules responsible for mediating entry of immune cells from blood circulation into LNs [99]. Recently, using targeted antibody-NIR-II probes, in vivo NIR-IIc confocal microscopy performed non-invasive through-tissue molecular imaging of HEVs, $CD169^+$ subcapsular sinus macrophages and $CD3^+$ T cells in the inguinal LNs of mice (Fig 3b) [12].

We employed NIR-II molecular imaging for assessing the immune responses of mice to immunotherapy. The different fluorescence lifetimes of ErNPs (~ 4.6 ms, emission ~ 1600 nm) and QDb (~ 46 ms, emission ~ 1600 nm) were exploited for in vivo two-plex NIR-IIb molecular imaging of PD-L1 and CD8, revealing the accumulation of CD8+ cytotoxic lymphocytes (CTLs) in the CT26 tumor upon treatment by anti-PD-L1 conjugated to ErNPs (Fig. 4d) [23]. Wide-field imaging and structured-illumination LSM were used for multiplex and multiscale molecular imaging of the CT26 tumor microenvironment in mice [26], for longitudinal tracking

of CD4, CD8, and OX40 at the single-cell level in response to immunotherapeutic CpG and OX40 antibody treatment by intratumoral injection.

Recently, a cancer nanovaccine was developed by conjugating ovalbumin (OVA) covalently and class-B cytosine–phosphate–guanine (CpG B) electrostatically to pErNP [29]. Upon subcutaneous injection, NIR-IIb imaging revealed trafficking of the nanovaccine, rapidly migrating to inguinal LNs through lymphatic vessels (Fig. 4e). Two doses of vaccination led to tumor eradication and cure/survival of mice. Wide-field imaging and structured-illumination LSM revealed abundant OVA antigen-specific CD8+ CTLs recruited to the tumor in the treated mouse (Fig. 4f). This was the first-time in vivo imaging of antigen specific CTLs was performed to correlate with immunotherapeutic effects of cancer vaccines (Fig. 4g).

NIR-II functional imaging. Functional imaging to probe the environmental parameters and cellular responses to stimulus is another exciting direction of in vivo NIR-II imaging, examples include NIR-II fluorescent molecules responding to external stimulus or environment, such as pH [65], redox species [100], nitroreductase [101], *Aβ* plaques [102] and cell endocytosis [103]. A unimolecular NIR-II chemiluminescence probe for H_2S was constructed by conjugating Schaap's dioxetane with a donor-acceptor core [104]. A more recent advancement is NIR-IIb imaging of oxyhemoglobin saturation (sO_2) in blood vessels based on the absorption difference between oxyhemoglobin and deoxyhemoglobin at specific excitation wavelengths (650, 808, and 980 nm) of pErNPs, enabling visualization of the sO_2 levels in tumor-associated vessels (Fig. 4h) [105]. Atomically precise NIR-II Au_{22} clusters with strong NIR-II fluorescence exhibits potent enzyme-mimetic activities, promising for early intervention of oxidative stress [43].

NIR-II imaging-guided surgery. Preclinical NIR-II imaging for intraoperative navigation is an active area of research towards potential clinical translations. Surgical removal of tumors (e.g. glioblastoma [18], pancreatic tumor [106], colorectal tumor [20], ovarian tumor [107] and breast tumor [94]) navigated by NIR-II imaging showed high promise. NIR-IIb molecular imaging of tumors using ErNP-TRC105 targeting tumor vasculature angiogenesis afforded tumor-to-muscle signal ratio up to ~ 300, allowing high-precision image-guided tumor resection down to few-cell level [28]. A recent work showed successful surgical removal of LNs labeled with QDb, achieving high LN to muscle ratios of ~ 200 [94]. In another work, NIR-II imaging-guided surgery led to complete resection of severe inflammatory bowels and ensured a secure surgical anastomosis by using AIE nanoprobes [108].

5. Towards clinical imaging

For any successful clinical translation of NIR-II fluorescence imaging, it is imperative to develop contrast agents that are safe for use in humans. Several groups found that traditional NIR-I organic dyes such as ICG and IRDye800CW exhibited emission tails into the NIR-II window [34,109] and can be utilized for NIR-II imaging to benefit from reduced light scattering and high imaging contrast and resolution. Since ICG is a Food and Drug Administration (FDA)-approved fluorophore, clinical trials of NIR-II imaging with ICG in human patients is of relatively low risk, but requires switching to an InGaAs based imaging system that has not gone through rigorous regulatory approval. Along this line, NIR-II fluorescence-guided

surgical resection of liver tumors in human patients was successfully performed after intravenous injection of ICG with a dose of 0.5 mg kg^{-1}, demonstrating a higher tumor detection sensitivity and rate than imaging in the NIR-I region (Fig. 5a) [96]. However, the ICG is a non-targeted probe, making false positives of tumors as it accumulates in other tissues [96]. Active tumor targeting for imaging guided surgery has clinically tested bioconjugates of IRDye800CW in NIR-I window [34]. IRDye800CW-conjugates exhibiting tail emission beyond 1000 nm, has potential for better determination of tumor margins [28].

Another promising direction of clinical translation is NIR-II imaging of perfusion. NIR-II imaging of ICG-tagged blood has been used to observe anastomotic vessels and the salvaged distal limbs [110]. It allowed observation of skin perforator vessels at the deep fascial level (Fig. 5b) and revascularization (Fig. 5c) before and after flap transplantation, respectively, with higher contrast, better resolution, and a longer duration of observation than NIR-I imaging [110].

Clinical trials of SWIR imaging using a label-free approach by exploiting the absorption properties of water were reported [111]. One example is the otoscope which uses the negative contrast of the water absorption band at 1480 nm to detect fluid in the middle ear [111].

6. Outlook and future directions

Probes and fluorophores. Currently organic NIR-II fluorophores with high absorptivity, QY and aqueous solubility, and ability of renal excretion and conjugation to target ligands are still rare. Molecules emitting predominantly in the NIR-IIb sub-window are also desired to compete with nanoprobes based on inorganic QDs and rare-earth nanoparticles. Another major challenge is the synthesis of functional NIR-II fluorophores with optical properties sensitive to environment and stimulus, especially for imaging-based sensing of pH, gas molecules, Ca^{2+} and other ions, and voltages and action potentials across ion channels of neurons.

The wide emission spectra of NIR-II fluorophores (FWHM = ~ 75-290 nm) have limited multiplexed imaging [18-21,27,36,37,42,112]. Multiplexed molecular imaging can be expanded by employing multi-color probes with different narrow-band emissions, probes with different excitation wavelengths, and probes with different fluorescence/luminescence lifetimes, all conjugated to molecular specific ligands to target different molecules in a body. For inorganic based nanoparticles, it is desired to have narrow emission widths across the 1000-2300 nm range with little spectral overlapping. Currently aqueous soluble, biocompatible NIR-IId probes (emission peak ~ 2200 nm) are lacking. Developing NIR-II probes with tunable fluorescence lifetime is another important approach to increase multiplexed molecular imaging [23] in vivo and should be pursued further. Thus far three-plex NIR-IIb imaging has been realized by combining continuous wave and lifetime imaging using QDs and rare-earth nanoparticles [29].

Developing genetically engineered NIR-II fluorescent proteins has been a daunting challenge thus far, and the success of which would mirror the GFP revolution, and undoubtedly boost the NIR-II field and lead to much more broad adoption of the imaging modality by biologists and medical scientists. NIR-II fluorescent proteins exist in nature, and several purple photosynthetic bacteria, including *blastochloris tepida*, *blastochloris viridis*, and

halorhodospira halochloris, possess bacteriochlorophyll *b*-based light harvesting complexes, exhibiting absorption and fluorescence in the NIR-II range [113]. Among them, light-harvesting 1–reaction center (LH1–RC) complex from *blastochloris viridis* has been observed to emit fluorescence with peak in NIR-II window [113], opening up opportunities for the development of NIR-II fluorescent proteins, but these very large protein complexes are still very difficult to use in genetic labelling strategies in mammalian cells [114].

NIR-II imaging devices and methods. New camera technologies with high sensitivity, low noise, broad spectral range spanning 1000 – 2300 nm and greater pixel numbers are important to enhance the NIR-II imaging performances and capabilities. High quantum-efficiency image intensifiers in the NIR-II range are needed for time-resolved/ultra-fast imaging and for weak fluorescence detection/imaging. Better cameras for NIR-IIc and NIR-IId imaging beyond InGaAs are needed for optimizing the benefit of in vivo fluorescence imaging in 2D wide-field and 3D light-sheet microscopy modes. Point detectors such as SNSPDs enabled high resolution deep tissue confocal microscopy in the NIR-IIc sub-window, but remains a challenge for the ~ 2200 nm NIR-IId range with low dark noise.

To push the resolution limit, it is desired to introduce optical super-resolution methods to microscopic imaging in the NIR-II window, similar to the approaches developed for the visible range such as non-linear SIM, stochastic optical reconstruction microscopy (STORM), photoactivated localization microscopy (PALM) and stimulated emission depletion (STED) microscopy. To realize these, specially designed NIR-II fluorescent probes and low-light sensitive detectors are required.

It is an interesting and exciting direction to invoke deep learning and artificial intelligence (AI) to enhance NIR-II fluorescence imaging. Recently, the cycle generative adversarial network (CycleGAN) was used to transform a blurred in vivo NIR-I or NIR-IIa image to a much higher-clarity image resembling NIR-IIb image [115]. Training with experimental data in a higher sub-window (e.g., NIR-IIc) could be used for machine learning, and then applied to transform and improve images acquired in the lower sub-window (e.g., NIR-IIb). AI approaches could address the problems of scarcity of probes [115] and affordability of high-end expensive cameras in the higher sub-windows, enabling noise reduction and sensitivity enhancement.

Clinical translation. Preclinical in vivo NIR-II fluorescence imaging has accumulated a large body of promising results for potential clinical translations. However, a major hurdle is the lack of clinically proven high performance NIR-II fluorophores or nanoprobes that are safe and have favorable pharmacokinetics for human use. Although FDA-approved ICG has high safety track record and exhibit tail fluorescence into the NIR-II window, the emission is mostly in the < 1200 nm range and imaging still suffers from substantial light scattering and high background. ICG also lacks functional groups for conjugation to target ligands and cannot be used for molecular imaging. Alternative dyes or probes are needed with a similar safety profile as ICG, with longer wavelength emission ideally in the NIR-IIb sub-window.

Among inorganic probes, rare-earth down-conversion nanoparticles are bright emitters for the high performing (low scattering, low autofluorescence) NIR-IIb imaging window, and have afforded excellent molecular imaging agents. Similar composition up-conversion nanoparticles

have proven highly safe to mice preclinically. However, clinical translation is uncertain due to probe scaling up issues and the lack of safety data from clinical settings. Quantum dots are even more challenging due to toxic elements. Another highly promising NIR-II probe is molecular gold clusters such as Au_{25}GSH and Au_{25}PC, as Au is widely accepted as a safe element, the clusters are rapidly renal excreted, exhibiting little non-specific tissue binding/uptake, and have shown higher performance in NIR-II LNs imaging than ICG [27]. Regardless, the clinical translation of any NIR-II agent must undergo rigorous phase I to III clinical trials for pharmacokinetics, toxicity, stability, side-effects/risks to humans and proof of benefits [116,117].

Standardization of NIR-II imaging system is another key step towards clinical translation. A set of characteristics of image devices for clinic use have been suggested in order to meet the requirements of the operating-room environment and clinical workflow [118]. Although originally intended for the evaluation of NIR-I fluorescence guided surgery systems, these criteria can provide a guide to future clinical NIR-II imaging devices, including (1) overlay of white-light and fluorescence images in real-time, (2) operation within surgical lighting; (3) high sensitivity, (4) in situ quantitative capabilities, (5) concurrent multi-plex fluorescence imaging and (6) maximized ergonomic utility for surgery [118]. The standardization for NIR-II imagers and contrast agents will accelerate regulatory approval, optimize device development, guarantee product quality, standardize clinical trials and reduce the risk [116,117].

The NIR-II imaging enabled tumor resection down to few-cell level with zero background [28]. Under this resolution, manual resection/surgical operation by hand could be challenging. We envisage that the combination of NIR-II imaging and surgical robots could become a powerful tool for precision medicine.

Competing interests

The authors declare no competing interests.

Materials & Correspondence

All relevant data are available from H. Dai upon reasonable request.

References

1 Genack, A. Z., Chabanov, A. A., Sebbah, P. & van Tiggelen, B. A. in *Encyclopedia of Condensed Matter Physics* (eds Franco Bassani, Gerald L. Liedl, & Peter Wyder) 307-317 (Elsevier, 2005).
2 Shi, L. & Alfano, R. R. *Deep imaging in tissue and biomedical materials: using linear and nonlinear optical methods*. (CRC Press, 2017).
3 Jacques, S. L. Optical properties of biological tissues: a review. *Phys. Med. Biol.* **58**, R37 (2013).
4 Hong, G., Antaris, A. L. & Dai, H. Near-infrared fluorophores for biomedical imaging. *Nat. Biomed. Eng.* **1**, 0010 (2017).
5 Hong, G. *et al.* Through-skull fluorescence imaging of the brain in a new near-infrared window. *Nat. Photonics* **8**, 723-730 (2014).
6 Weissleder, R. A clearer vision for in vivo imaging. *Nat. Biotechnol.* **19**, 316-317 (2001).
7 Friebel, M., Helfmann, J., Netz, U. & Meinke, M. Influence of oxygen saturation on the optical scattering properties of human red blood cells in the spectral range 250 to 2000 nm. *J. Biomed. Opt.* **14**, 034001 (2009).

8 Reinhart, M. B., Huntington, C. R., Blair, L. J., Heniford, B. T. & Augenstein, V. A. Indocyanine green:historical context, current applications, and future considerations. *Surg. Innov.* **23**, 166-175 (2016).
9 Smith, A. M., Mancini, M. C. & Nie, S. Second window for in vivo imaging. *Nat. Nanotechnol.* **4**, 710-711 (2009).
10 Diao, S. *et al.* Biological imaging without autofluorescence in the second near-infrared region. *Nano Res.* **8**, 3027-3034 (2015).
11 Welsher, K. *et al.* A route to brightly fluorescent carbon nanotubes for near-infrared imaging in mice. *Nat. Nanotechnol.* **4**, 773-780 (2009).
12 Wang, F. *et al.* In vivo non-invasive confocal fluorescence imaging beyond 1,700 nm using superconducting nanowire single-photon detectors. *Nature Nanotechnology* **17**, 653-660 (2022).
13 Liu, Z., Tabakman, S., Welsher, K. & Dai, H. Carbon nanotubes in biology and medicine: In vitro and in vivo detection, imaging and drug delivery. *Nano Res.* **2**, 85-120 (2009).
14 Welsher, K., Sherlock, S. P. & Dai, H. Deep-tissue anatomical imaging of mice using carbon nanotube fluorophores in the second near-infrared window. *P. Natl. Acad. Sci. USA* **108**, 8943-8948 (2011).
15 Hong, G. *et al.* Multifunctional in vivo vascular imaging using near-infrared II fluorescence. *Nat. Med.* **18**, 1841-1846 (2012).
16 Hong, G. *et al.* In vivo fluorescence imaging with Ag2S quantum dots in the second near-infrared region. *Angew. Chem. Int. Edit.* **51**, 9818-9821 (2012).
17 Diao, S. *et al.* Fluorescence imaging in vivo at wavelengths beyond 1500 nm. *Angew. Chem. Int. Edit.* **54**, 14758-14762 (2015).
18 Antaris, A. L. *et al.* A small-molecule dye for NIR-II imaging. *Nat. Mater.* **15**, 235-242 (2016).
19 Zhong, Y. *et al.* Boosting the down-shifting luminescence of rare-earth nanocrystals for biological imaging beyond 1500 nm. *Nat. Commun.* **8**, 737 (2017).
20 Wan, H. *et al.* Developing a bright NIR-II fluorophore with fast renal excretion and its application in molecular imaging of immune checkpoint PD-L1. *Adv. Funct. Mater.* **28**, 1804956 (2018).
21 Zhang, M. *et al.* Bright quantum dots emitting at ~1,600 nm in the NIR-IIb window for deep tissue fluorescence imaging. *P. Natl. Acad. Sci. USA* **115**, 6590-6595 (2018).
22 Ma, Z. *et al.* A theranostic agent for cancer therapy and imaging in the second near-infrared window. *Nano Res.* **12**, 273-279 (2019).
23 Zhong, Y. *et al.* In vivo molecular imaging for immunotherapy using ultra-bright near-infrared-IIb rare-earth nanoparticles. *Nat. Biotechnol.* **37**, 1322-1331 (2019).
24 Wang, F. *et al.* Light-sheet microscopy in the near-infrared II window. *Nat. Methods* **16**, 545-552 (2019).
25 Ma, Z. *et al.* Cross-link-functionalized nanoparticles for rapid excretion in nanotheranostic applications. *Angew. Chem. Int. Edit.* **59**, 20552-20560 (2020).
26 Wang, F. *et al.* In vivo NIR-II structured-illumination light-sheet microscopy. *P. Natl. Acad. Sci. USA* **118**, e2023888118 (2021).
27 Baghdasaryan, A. *et al.* Phosphorylcholine-conjugated gold-molecular clusters improve signal for Lymph Node NIR-II fluorescence imaging in preclinical cancer models. *Nat. Commun.* **13**, 5613 (2022).
28 Wang, F. *et al.* High-precision tumor resection down to few-cell level guided by NIR-IIb molecular fluorescence imaging. *P. Natl. Acad. Sci. USA* **119**, e2123111119 (2022).
29 Ren, F. *et al.* Shortwave-infrared-light-emitting probes for the in vivo tracking of cancer vaccines and the elicited immune responses. *Nat. Biomed. Eng.* (2023, https://doi.org/10.1038/s41551-023-01083-5).
30 Carr, J. A., Aellen, M., Franke, D., So, P. T. C., Bruns, O. T. & Bawendi, M. G. Absorption by water increases fluorescence image contrast of biological tissue in the shortwave infrared. *P. Natl. Acad. Sci. USA* **115**, 9080-9085 (2018).
31 Yoo, K. M., Liu, F. & Alfano, R. R. Imaging through a scattering wall using absorption. *Opt. Lett.* **16**, 1068-1070 (1991).
32 Shao, W. *et al.* Tunable narrow band emissions from dye-sensitized core/shell/shell nanocrystals in the second near-infrared biological window. *J. Am. Chem. Soc.* **138**, 16192-16195 (2016).

33 Wei, Y.-C. *et al.* Overcoming the energy gap law in near-infrared OLEDs by exciton–vibration decoupling. *Nat. Photonics* **14**, 570-577 (2020).
34 Zhu, S., Tian, R., Antaris, A. L., Chen, X. & Dai, H. Near-infrared-II molecular dyes for cancer imaging and surgery. *Adv. Mater.* **31**, 1900321 (2019).
35 Chen, R. J., Zhang, Y., Wang, D. & Dai, H. Noncovalent sidewall functionalization of single-walled carbon nanotubes for protein immobilization. *J. Am. Chem. Soc.* **123**, 3838-3839 (2001).
36 Zhang, Y. *et al.* Ag_2S quantum dot: a bright and biocompatible fluorescent nanoprobe in the second near-infrared window. *ACS Nano* **6**, 3695-3702 (2012).
37 Bruns, O. T. *et al.* Next-generation in vivo optical imaging with short-wave infrared quantum dots. *Nat. Biomed. Eng.* **1**, 0056 (2017).
38 Zhong, Y. & Dai, H. A mini-review on rare-earth down-conversion nanoparticles for NIR-II imaging of biological systems. *Nano Res.* **13**, 1281-1294 (2020).
39 Gu, Y. *et al.* High-sensitivity imaging of time-domain near-infrared light transducer. *Nat. Photonics* **13**, 525-531 (2019).
40 Pei, P. *et al.* X-ray-activated persistent luminescence nanomaterials for NIR-II imaging. *Nat. Nanotechnol.* **16**, 1011-1018 (2021).
41 Yang, Y. *et al.* Fluorescence-amplified nanocrystals in the second near-infrared window for in vivo real-time dynamic multiplexed imaging. *Nat. Nanotechnol.* **18**, 1195–1204 (2023).
42 Chen, Y. *et al.* Shortwave Infrared in Vivo Imaging with Gold Nanoclusters. *Nano Lett.* **17**, 6330-6334 (2017).
43 Ma, H. *et al.* Bioactive NIR-II gold clusters for three-dimensional imaging and acute inflammation inhibition. *Sci. Adv.* **9**, eadh7828 (2023).
44 Cosco, E. D. *et al.* Shortwave infrared polymethine fluorophores matched to excitation lasers enable non-invasive, multicolour in vivo imaging in real time. *Nat. Chem.* **12**, 1123-1130 (2020).
45 Sun, C. *et al.* J-aggregates of cyanine dye for NIR-II in vivo dynamic vascular imaging beyond 1500 nm. *J. Am. Chem. Soc.* **141**, 19221-19225 (2019).
46 Yang, Q. *et al.* Rational design of molecular fluorophores for biological imaging in the NIR-II window. *Adv. Mater.* **29**, 1605497 (2017).
47 Zhu, X. *et al.* High brightness NIR-II nanofluorophores based on fused-ring acceptor molecules. *Nano Res.* **13**, 2570-2575 (2020).
48 Yao, C. *et al.* A bright, renal-clearable NIR-II brush macromolecular probe with long blood circulation time for kidney disease bioimaging. *Angew. Chem. Int. Edit.* **61**, e202114273 (2022).
49 Qin, Z. *et al.* NIRII-HDs: a versatile platform for developing activatable NIR-II fluorogenic probes for reliable in vivo analyte sensing. *Angew. Chem. Int. Edit.* **61**, e202201541 (2022).
50 Wang, T. *et al.* A hybrid erbium(III)–bacteriochlorin near-infrared probe for multiplexed biomedical imaging. *Nat. Mater.* **20**, 1571-1578 (2021).
51 Lei, Z. *et al.* Stable, Wavelength-Tunable Fluorescent Dyes in the NIR-II Region for In Vivo High-Contrast Bioimaging and Multiplexed Biosensing. *Angewandte Chemie International Edition* **58**, 8166-8171 (2019).
52 Liu, S. *et al.* Incorporation of planar blocks into twisted skeletons: boosting brightness of fluorophores for bioimaging beyond 1500 nanometer. *ACS Nano* **14**, 14228-14239 (2020).
53 Liu, C., Wang, X., Zhu, X., Ma, R., Lin, Q. & Liang, Y. 3,4-Ethylenedithio thiophene donor for NIR-II fluorophores with improved quantum yields. *Mater. Chem. Front.* **7**, 2419-2425 (2023).
54 Ma, H. *et al.* Propylenedioxy Thiophene Donor to Achieve NIR-II Molecular Fluorophores with Enhanced Brightness. *Chemistry of Materials* **32**, 2061-2069 (2020).
55 Yang, Q. *et al.* Donor engineering for NIR-II molecular fluorophores with enhanced fluorescent performance. *J. Am. Chem. Soc.* **140**, 1715-1724 (2018).
56 Huang, J. *et al.* Renal-clearable Molecular Semiconductor for Second Near-Infrared Fluorescence Imaging of Kidney Dysfunction. *Angewandte Chemie International Edition* **58**, 15120-15127 (2019).
57 Shcherbakova, D. M. & Verkhusha, V. V. Near-infrared fluorescent proteins for multicolor in vivo imaging. *Nat. Methods* **10**, 751-754 (2013).
58 Oliinyk, O. S., Chernov, K. G. & Verkhusha, V. V. Bacterial phytochromes, cyanobacteriochromes and allophycocyanins as a source of near-infrared fluorescent probes. *Int. J. Mol. Sci.* **18**, 1691 (2017).

59 Chen, M. *et al.* Long-term monitoring of intravital biological processes using fluorescent protein-assisted NIR-II imaging. *Nat. Commun.* **13**, 6643 (2022).
60 Oliinyk, O. S. *et al.* Deep-tissue SWIR imaging using rationally designed small red-shifted near-infrared fluorescent protein. *Nat. Methods* **20**, 70-74 (2023).
61 Naczynski, D. J. *et al.* X-ray-induced shortwave infrared biomedical imaging using rare-earth nanoprobes. *Nano Lett.* **15**, 96-102 (2015).
62 Cao, X. *et al.* Cherenkov excited short-wavelength infrared fluorescence imaging in vivo with external beam radiation. *J. Biomed. Opt.* **24**, 051405 (2018).
63 Shen, H. *et al.* Rational design of NIR-II AIEgens with ultrahigh quantum yields for photo- and chemiluminescence imaging. *J. Am. Chem. Soc.* **144**, 15391-15402 (2022).
64 Lu, L. *et al.* NIR-II bioluminescence for in vivo high contrast imaging and in situ ATP-mediated metastases tracing. *Nat. Commun.* **11**, 4192 (2020).
65 Wang, S. *et al.* Anti-quenching NIR-II molecular fluorophores for in vivo high-contrast imaging and pH sensing. *Nat. Commun.* **10**, 1058 (2019).
66 Starosolski, Z., Bhavane, R., Ghaghada, K. B., Vasudevan, S. A., Kaay, A. & Annapragada, A. Indocyanine green fluorescence in second near-infrared (NIR-II) window. *PLOS ONE* **12**, e0187563 (2017).
67 Ren, T.-B. *et al.* A general strategy for development of activatable NIR-II fluorescent probes for in vivo high-contrast bioimaging. *Angew. Chem. Int. Edit.* **60**, 800-805 (2021).
68 Wang, Z. *et al.* Dynamically monitoring lymphatic and vascular systems in physiological and pathological conditions of a swine model via a portable NIR-II imaging system with ICG. *Int. J. Med. Sci.* **19**, 1864-1874 (2022).
69 Xue, D. *et al.* Structural and functional NIR-II fluorescence bioimaging in urinary system via clinically approved dye methylene blue. *Engineering* **22**, 149-158 (2023).
70 Chang, Y. *et al.* Bright Tm3+-based downshifting luminescence nanoprobe operating around 1800 nm for NIR-IIb and c bioimaging. *Nat. Commun.* **14**, 1079 (2023).
71 Arús, B. A. *et al.* Shortwave infrared fluorescence imaging of peripheral organs in awake and freely moving mice. *Front. Neurosci.* **17** (2023, https://doi.org/10.3389/fnins.2023.1135494).
72 Kim, T., O'Brien, C., Choi, H. S. & Jeong, M. Y. Fluorescence molecular imaging systems for intraoperative image-guided surgery. *Appl. Spectrosc. Rev.* **53**, 349-359 (2018).
73 Wan, H. *et al.* A bright organic NIR-II nanofluorophore for three-dimensional imaging into biological tissues. *Nat. Commun.* **9**, 1171 (2018).
74 Yu, W. *et al.* NIR-II fluorescence in vivo confocal microscopy with aggregation-induced emission dots. *Sci. Bull.* **64**, 410-416 (2019).
75 Yu, J. *et al.* Intravital confocal fluorescence lifetime imaging microscopy in the second near-infrared window. *Opt. Lett.* **45**, 3305-3308 (2020).
76 Xia, F. *et al.* Short-wave infrared confocal fluorescence imaging of deep mouse brain with a superconducting nanowire single-photon detector. *ACS Photonics* **8**, 2800-2810 (2021).
77 Kobat, D., Horton, N. & Xu, C. In vivo two-photon microscopy to 1.6-mm depth in mouse cortex. *J. Biomed. Opt.* **16**, 106014 (2011).
78 Horton, N. G. *et al.* In vivo three-photon microscopy of subcortical structures within an intact mouse brain. *Nat. Photonics* **7**, 205-209 (2013).
79 Gu, M., Gan, X., Kisteman, A. & Xu, M. G. Comparison of penetration depth between two-photon excitation and single-photon excitation in imaging through turbid tissue media. *Appl. Phys. Lett.* **77**, 1551-1553 (2000).
80 Huisken, J., Swoger, J., Del Bene, F., Wittbrodt, J. & Stelzer, E. H. K. Optical sectioning deep inside live embryos by selective plane illumination microscopy. *Science* **305**, 1007-1009 (2004).
81 Liu, T.-L. *et al.* Observing the cell in its native state: Imaging subcellular dynamics in multicellular organisms. *Science* **360**, eaaq1392 (2018).
82 Yu, H. *et al.* in *Biophotonics Congress: Biomedical Optics Congress 2018 (Microscopy/Translational/Brain/OTS).* BF3C.3 (Optica Publishing Group).
83 Olarte, O. E. *et al.* Image formation by linear and nonlinear digital scanned light-sheet fluorescence microscopy with Gaussian and Bessel beam profiles. *Biomed. Opt. Express* **3**, 1492-1505 (2012).

84 Nylk, J. *et al.* Light-sheet microscopy with attenuation-compensated propagation-invariant beams. *Sci. Adv.* **4**, eaar4817 (2018).
85 Herisson, F. *et al.* Direct vascular channels connect skull bone marrow and the brain surface enabling myeloid cell migration. *Nat. Neurosci.* **21**, 1209-1217 (2018).
86 Wang, F. *et al.* Scanning superlens microscopy for non-invasive large field-of-view visible light nanoscale imaging. *Nat. Commun.* **7**, 13748 (2016).
87 Liu, P. *et al.* Airy beam assisted NIR-II light-sheet microscopy. *Nano Today* **47**, 101628 (2022).
88 Gustafsson, M. G. L. Nonlinear structured-illumination microscopy: Wide-field fluorescence imaging with theoretically unlimited resolution. *Proceedings of the National Academy of Sciences of the United States of America* **102**, 13081-13086 (2005).
89 Hong, G. *et al.* Near-Infrared II fluorescence for imaging hindlimb vessel regeneration with dynamic tissue perfusion measurement. *Circ.-Cardiovasc. Imag.* **7**, 517-525 (2014).
90 Qi, J. *et al.* Real-time and high-resolution bioimaging with bright aggregation-induced emission dots in short-wave infrared region. *Adv. Mater.* **30**, 1706856 (2018).
91 Liu, H. *et al.* Atomic-precision gold clusters for NIR-II imaging. *Adv. Mater.* **31**, 1901015 (2019).
92 Zhang, X.-D. *et al.* Traumatic brain injury imaging in the second near-infrared window with a molecular fluorophore. *Adv. Mater.* **28**, 6872-6879 (2016).
93 Chatterjee, A., Serniak, N. & Czerniecki, B. J. Sentinel lymph node biopsy in breast cancer: a work in progress. *Cancer J.* **21** (2015).
94 Tian, R. *et al.* Multiplexed NIR-II probes for lymph node-invaded cancer detection and imaging-guided surgery. *Adv. Mater.* **32**, 1907365 (2020).
95 Li, M. *et al.* Near-infrared-II ratiometric fluorescence probes for non-invasive detection and precise navigation surgery of metastatic sentinel lymph nodes. *Theranostics* **12**, 7191-7202 (2022).
96 Hu, Z. *et al.* First-in-human liver-tumour surgery guided by multispectral fluorescence imaging in the visible and near-infrared-I/II windows. *Nat. Biomed. Eng.* **4**, 259-271 (2020).
97 Morlandt, A. B. *et al.* Fluorescently labeled Cetuximab-IRDye800 for guided surgical excision of ameloblastoma: a proof of principle study. *J. Oral. Maxil. Surg.* **78**, 1736-1747 (2020).
98 Suo, Y. *et al.* NIR-II fluorescence endoscopy for targeted imaging of colorectal cancer. *Adv. Healthc. Mater.* **8**, 1900974 (2019).
99 Girard, J.-P., Moussion, C. & Förster, R. HEVs, lymphatics and homeostatic immune cell trafficking in lymph nodes. *Nat. Rev. Immunol.* **12**, 762-773 (2012).
100 He, L. *et al.* Engineering of reversible NIR-II redox-responsive fluorescent probes for imaging of inflammation in vivo. *Angew. Chem. Int. Edit.* **61**, e202211409 (2022).
101 Lan, Q., Yu, P., Yan, K., Li, X., Zhang, F. & Lei, Z. Polymethine molecular platform for ratiometric fluorescent probes in the second near-infrared window. *J. Am. Chem. Soc.* **144**, 21010-21015 (2022).
102 Miao, J. *et al.* An activatable NIR-II fluorescent reporter for in vivo imaging of Amyloid-β plaques. *Angew. Chem. Int. Edit.* **62**, e202216351 (2023).
103 He, Y. *et al.* NIR-II cell endocytosis-activated fluorescent probes for in vivo high-contrast bioimaging diagnostics. *Chem. Sci.* **12**, 10474-10482 (2021).
104 Chen, Z. *et al.* Design and synthesis of a small molecular NIR-II chemiluminescence probe for in vivo-activated H_2S imaging. *P. Natl. Acad. Sci. USA* **120**, e2205186120 (2023).
105 Fang, Z. *et al.* Oxyhaemoglobin saturation NIR-IIb imaging for assessing cancer metabolism and predicting the response to immunotherapy. *Nat. Nanotechnol.* (2023, https://doi.org/10.1038/s41565-023-01501-4).
106 Tian, R. *et al.* Rational design of a super-contrast NIR-II fluorophore affords high-performance NIR-II molecular imaging guided microsurgery. *Chem. Sci.* **10**, 326-332 (2019).
107 Wang, P. *et al.* NIR-II nanoprobes in-vivo assembly to improve image-guided surgery for metastatic ovarian cancer. *Nat. Commun.* **9**, 2898 (2018).
108 Fan, X. *et al.* Aggregation-induced emission (AIE) nanoparticles-assisted NIR-II fluorescence imaging-guided diagnosis and surgery for inflammatory bowel disease (IBD). *Adv. Healthc. Mater.* **10**, 2101043 (2021).
109 Antaris, A. L. *et al.* A high quantum yield molecule-protein complex fluorophore for near-infrared II imaging. *Nat. Commun.* **8**, 15269 (2017).

110 Wu, Y. *et al.* First clinical applications for the NIR-II imaging with ICG in microsurgery. *Front. Bioeng. Biotech.* **10** (2022).
111 Carr, J. A., Valdez, T. A., Bruns, O. T. & Bawendi, M. G. Using the shortwave infrared to image middle ear pathologies. *P. Natl. Acad. Sci. USA* **113**, 9989-9994 (2016).
112 Shi, X. *et al.* Zn-doping enhances the photoluminescence and stability of PbS quantum dots for in vivo high-resolution imaging in the NIR-II window. *Nano Res.* **13**, 2239-2245 (2020).
113 Magdaong, N. C. M., Niedzwiedzki, D. M., Goodson, C. & Blankenship, R. E. Carotenoid-to-bacteriochlorophyll energy transfer in the LH1–RC core complex of a bacteriochlorophyll b containing purple photosynthetic bacterium blastochloris viridis. *J. Phys. Chem. B* **120**, 5159-5171 (2016).
114 Chang, Z. *et al.* Near infrared-II fluorescent protein for in-vivo imaging. *bioRxiv*, 2022.2003.2004.482971 (2022).
115 Ma, Z., Wang, F., Wang, W., Zhong, Y. & Dai, H. Deep learning for in vivo near-infrared imaging. *P. Natl. Acad. Sci. USA* **118**, e2021446118 (2021).
116 Tummers, W. S. *et al.* Regulatory aspects of optical methods and exogenous targets for cancer detection. *Cancer. Res.* **77**, 2197-2206 (2017).
117 Scheuer, W., van Dam, G. M., Dobosz, M., Schwaiger, M. & Ntziachristos, V. Drug-based optical agents: infiltrating clinics at lower risk. *Sci. Transl. Med.* **4**, 134ps111-134ps111 (2012).
118 DSouza, A., Lin, H., Henderson, E., Samkoe, K. & Pogue, B. Review of fluorescence guided surgery systems: identification of key performance capabilities beyond indocyanine green imaging. *J. Biomed. Opt.* **21**, 080901 (2016).
119 Wang, M., Wu, C., Sinefeld, D., Li, B., Xia, F. & Xu, C. Comparing the effective attenuation lengths for long wavelength in vivo imaging of the mouse brain. *Biomed. Opt. Express* **9**, 3534-3543 (2018).

Acknowledgments

H. Dai acknowledges National Institutes of Health NIH DP1-NS-105737 as the sole funding source for Dai group's work reviewed in this publication.

Figure 1. Motivation for NIR-II fluorescence imaging. (**a**) Reduced scattering coefficients of different biological tissues and intralipid phantom with concentrations of 0.8% and 4.6% in the 400-3000 nm window. (**b**) The attenuation length ($1/(1/l_s+1/l_a)$) of brain tissue mimicked by 5% intralipid solution in the NIR-I and NIR-II windows, where l_s and l_a are scatter and attenuation lengths [12]. The stars in the graph denote the effective attenuation length of mouse brain that has been previously reported [78,119]. (**c**) Fluorescence imaging of a 50-μm capillary submerged at various depths in 5% intralipid by a wide-field system with a 2D InGaAs camera or a confocal microscope with SNSPDs. An 808-nm and a 1319-nm laser were used for NIR-IIb wide-field imaging and confocal microscopy, respectively. NIR-IIc confocal microscopy was performed with 1540-nm or 1650-nm excitations [12]. (**d**) Non-invasive NIR-I, NIR-IIa and NIR-IIb fluorescence imaging of cerebral vasculatures of mice [17].

Figure 2. NIR-II fluorescence probes. (**a**) The emission spectral ranges of different inorganic nanostructured NIR-II probes. (**b**) Schemes of SWNTs with proteins anchored on the surface via pyrene π-stacking [35]. (**c**) Emission spectrum and schematic design (inset) of NIR-IIc core-

shell PbS/CdS QDs [12]. (**d**) Schematic overview of InAs-based QDs coated with passivation shell [37]. (**e**) Schematic of the Tm^{3+}-doped cubic-phase core–shell-structured RENPs [41]. (**f**) Crystallographic representation of Au_{25} nanoclusters [27]. (**g**) Schematic illustration of the hydrophilic RENPs with P^3 coating cross-linking polymeric layers [23]. The example structures of NIR-II molecular fluorophores (**h**) polymethine (JuloFlav7 [44] and FD-1080 [45]), (**i**) donor-acceptor molecules (IR-FEP [46] and CPTIC-4F [47]), (**j**) BODIPY (FBPEG 912 [48]), (**k**) rhodamine (NIR-II-HD5-ALP [49]) and (**l**) metal-macrocycles complexes (EB766 [50]).

Figure 3. NIR-II imaging modalities. (**a**) Upper: schemes of NIR-II wide-field imaging systems for small animal imaging and image guided surgery. Bottom: the sensitivity range of different camera materials. (**b**) Left: a scheme of NIR-II confocal microscope. Middle: Non-invasive confocal microscopy of blood vessels (red) in NIR-IIa window and HEVs labelled by aMECA-79-QDc (green, QDc: NIR-IIc PbS QDs) in NIR-IIc window in an inguinal lymph node. Right: Confocal microscopy of $CD169^+$ macrophages (aCD169-QDa, QDa: NIR-IIa PbS QDs) and $CD3^+$ T cells (aCD3-QDc) in a inguinal lymph node [12]. (**c**) Upper: schemes of NIR-II light sheet microscopes with normal and oblique configurations and NIR-II structured-illumination LSM. Bottom-Left: Time-course recording of $PD\text{-}1^+$ cells (white circles) in a CT26 tumor labeled by anti-PD-1-PbS QDs at 20 frames per second by oblique LSM [24]. Bottom-Right: A higher-resolution NIR-II structured-illumination LSM of aCD4-ErNPs (red) and aOX40-QDb (green) in a CpG-treated tumor [26].

Figure 4. NIR-II preclinical imaging. (**a**) NIR-II PCA overlaid images showing arterial and venous vessels of a heathy mouse and a mouse with MCAO [5]. (**b**) NIR-II imaging of a brain tumor, arteries and veins [37]. (**c**) NIR-II imaging of sentinel LNs after injection of ICG and Au-PC [27]. (**d**) Two-plex NIR-IIb imaging of a mouse bearing CT-26 tumor at 24 h post intravenous injection of ErNPs-aPDL1 and PbS QDs-aCD8 [23]. (**e**) Time-course recording of vaccine trafficking pathways after injection of pErNP-OVA–CpG B [29]. (**f**) NIR-IIb imaging of mice bearing E.G-7 tumors with intratumoral injection of pErNP-OVA–CpG B or PBS [29]. (**g**) Treatment efficacy corresponding treatment in (**f**) [29]. (**h**) NIR-IIb imaging of sO_2. Upper: The relationship between sO_2 value and the ratio of fluorescence signals excited at 650 nm and 980 nm. Bottom: NIR-IIb sO_2 imaging of the perfusion of pErNP into 4T1 tumor [105].

Figure 5. NIR-II clinical imaging. (**a**) Upper: A schematic shows an example equipment for visible, NIR-I and NIR-II image-guided surgery for clinical tumor resection. Bottom: Intraoperative visible, NIR-I and NIR-II imaging of a tumor before and during tumor resection [96]. (**b**) Preoperative (Upper) NIR-I and (Bottom) NIR-II fluorescence imaging revealed four possible perforators after intravenous injection of ICG. NIR-II imaging resolved more perforators than traditional Doppler method. One of them overlapped with the Doppler location [110]. (**c**) Left: color image of human heel after flap transplantation. NIR-I (Middle) and NIR-II (Right) fluorescence imaging of flap perfusion and revascularization. NIR-II imaging enhanced visualization of revascularization compared to NIR-I imaging [110].

848

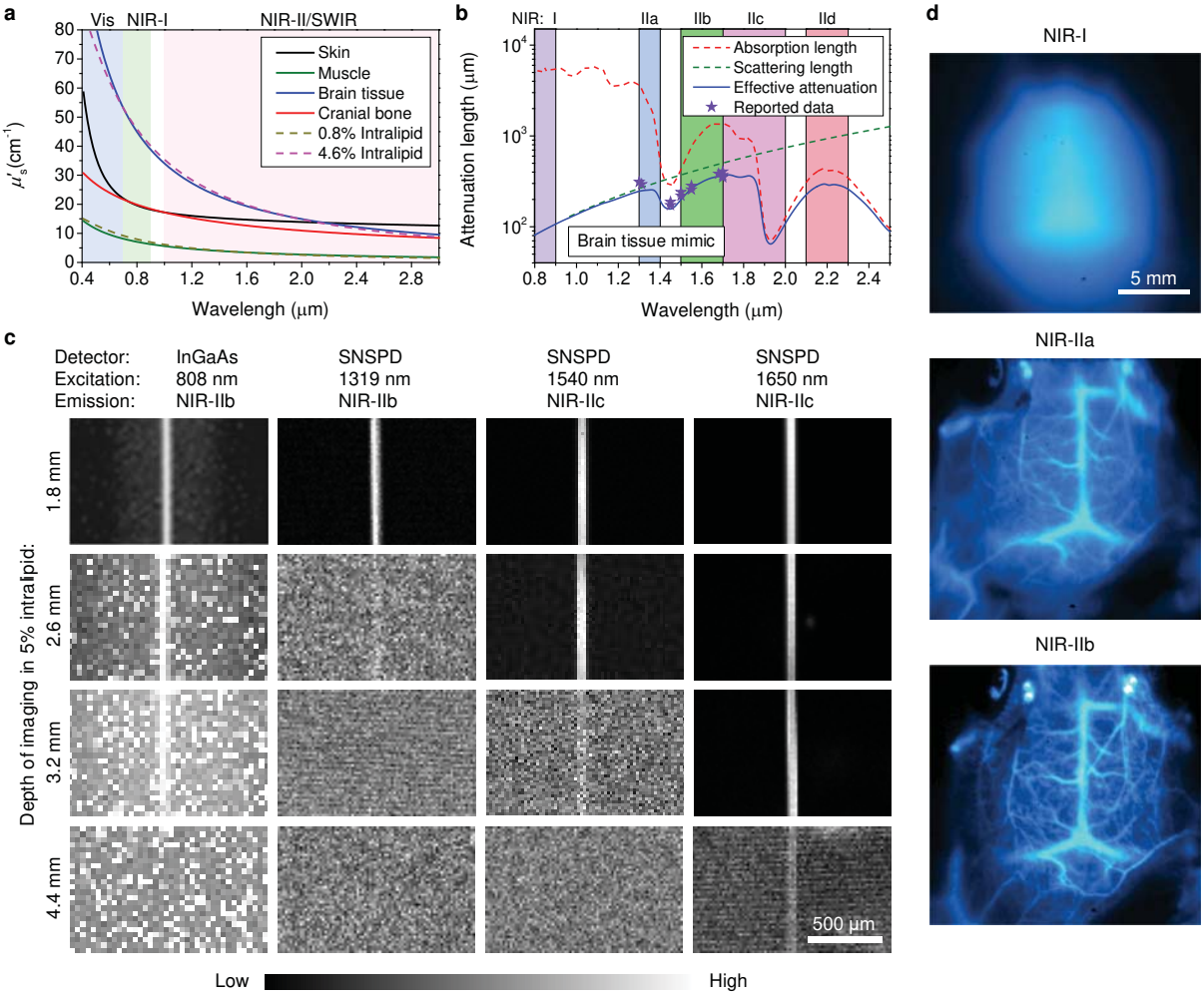
a
Vis
NIR-I
NIR-II/SWIR
Skin
Muscle
Brain tissue
Cranial bone
0.8% Intralipid
4.6% Intralipid
$\mu_s'(cm^{-1})$
Wavelength (μm)
b
NIR: I
IIa
IIb
IIc
IId
Absorption length
Scattering length
Effective attenuation
Reported data
Brain tissue mimic
Attenuation length (μm)
Wavelength (μm)
c
Detector: InGaAs SNSPD SNSPD SNSPD
Excitation: 808 nm 1319 nm 1540 nm 1650 nm
Emission: NIR-IIb NIR-IIb NIR-IIc NIR-IIc
Depth of imaging in 5% intralipid:
1.8 mm
2.6 mm
3.2 mm
4.4 mm
500 μm
Low
High
d
NIR-I
5 mm
NIR-IIa
NIR-IIb

Inorganic nanomaterials

Molecular fluorophores

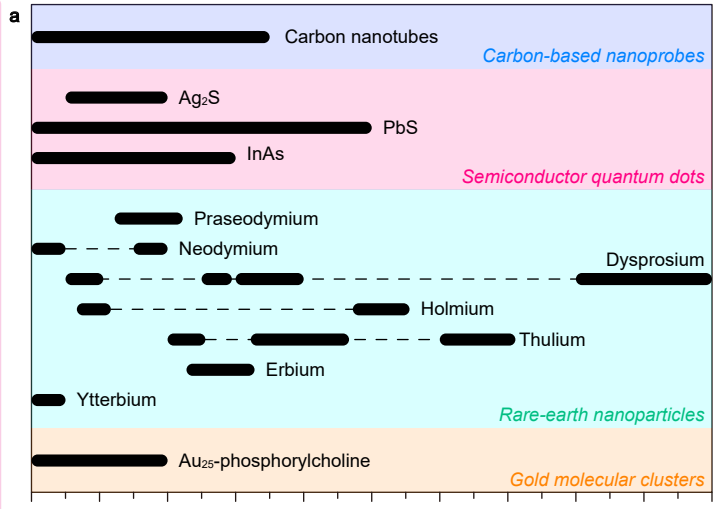

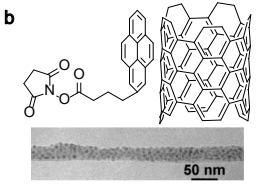

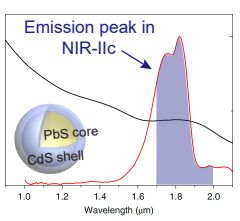

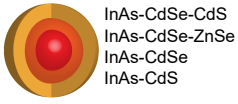

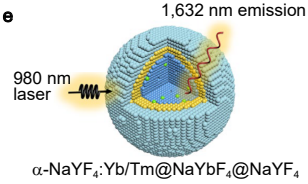

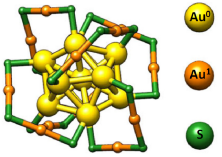

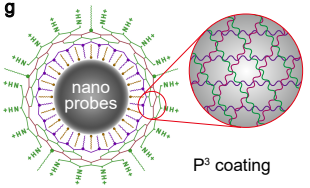

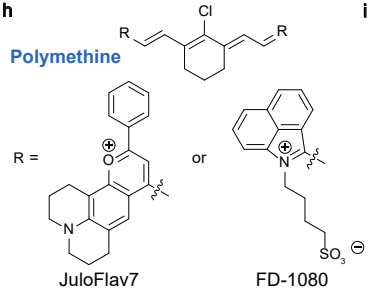

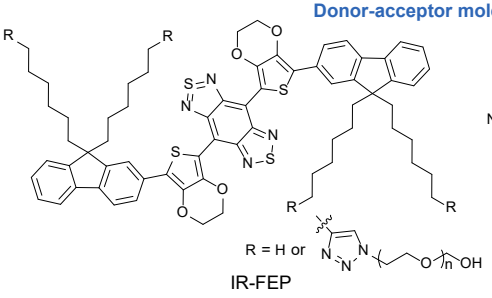

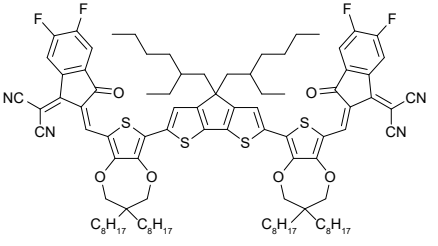

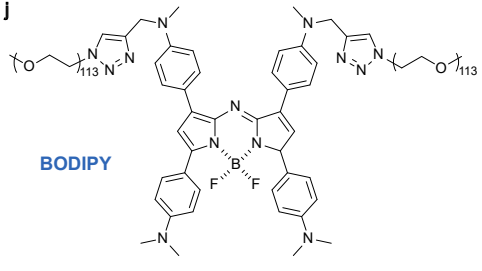

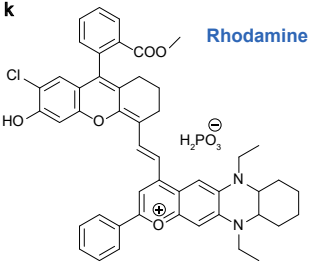

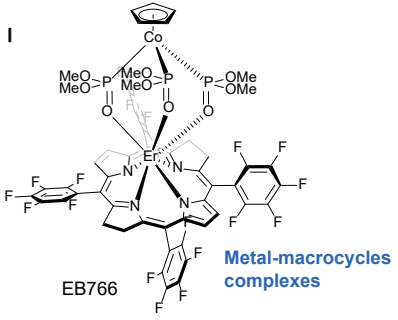

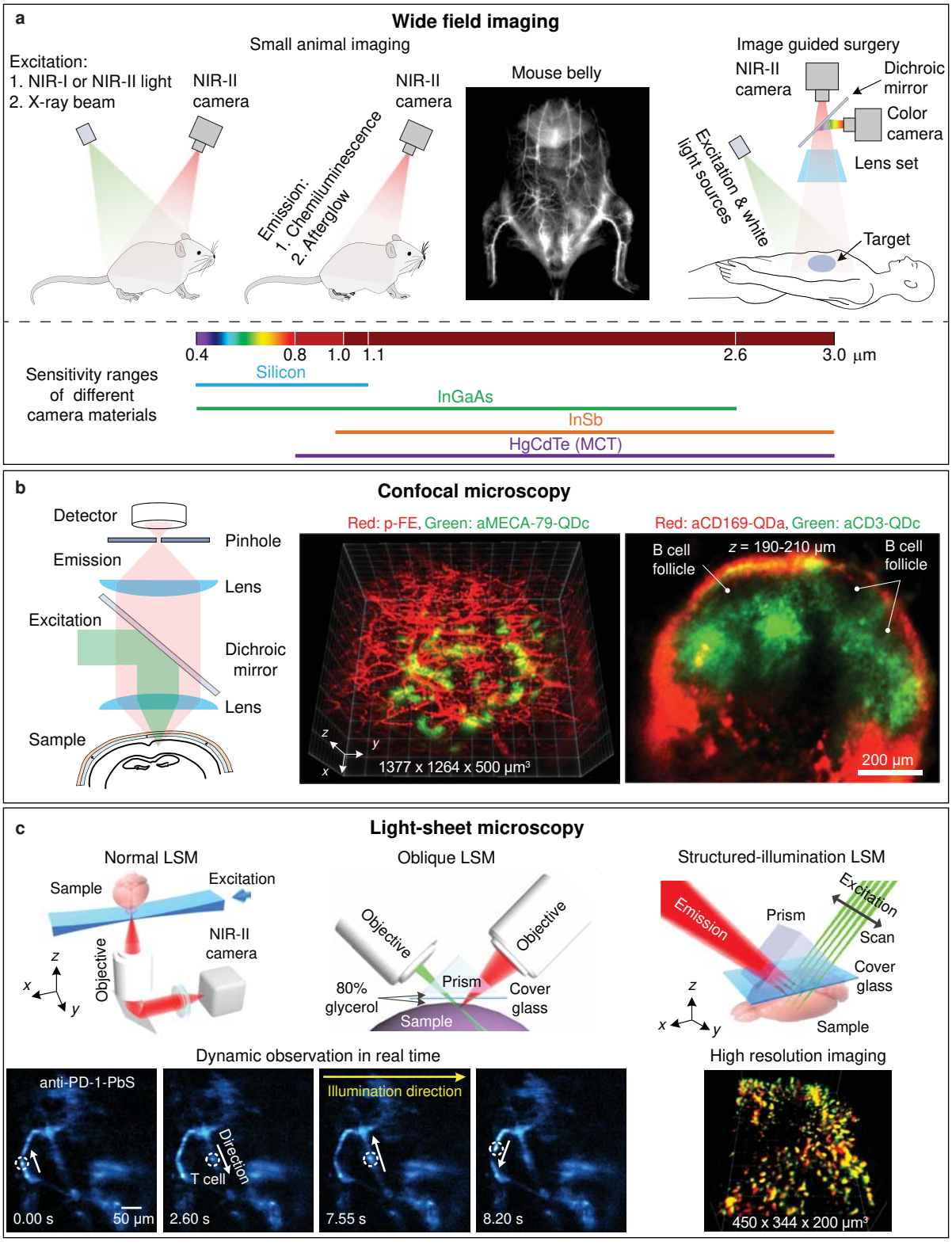
a
Wide field imaging
Small animal imaging
Excitation:
1. NIR-I or NIR-II light
2. X-ray beam
NIR-II camera
NIR-II camera
Emission:
1. Chemiluminescence
2. Afterglow
Mouse belly
Image guided surgery
NIR-II camera
Dichroic mirror
Color camera
Lens set
Excitation & white light sources
Target
0.4
0.8
1.0
1.1
2.6
3.0 μm
Sensitivity ranges of different camera materials
Silicon
InGaAs
InSb
HgCdTe (MCT)
b
Confocal microscopy
Detector
Pinhole
Emission
Lens
Excitation
Dichroic mirror
Lens
Sample
Red: p-FE, Green: aMECA-79-QDc
1377 x 1264 x 500 μm³
Red: aCD169-QDa, Green: aCD3-QDc
B cell follicle
z = 190-210 μm
B cell follicle
200 μm
c
Light-sheet microscopy
Normal LSM
Sample
Excitation
NIR-II camera
Objective
Oblique LSM
Objective
Objective
80% glycerol
Prism
Cover glass
Sample
Structured-illumination LSM
Emission
Prism
Excitation
Scan
Cover glass
Sample
Dynamic observation in real time
anti-PD-1-PbS
0.00 s
50 μm
T cell
Direction
2.60 s
Illumination direction
7.55 s
8.20 s
High resolution imaging
450 x 344 x 200 μm³

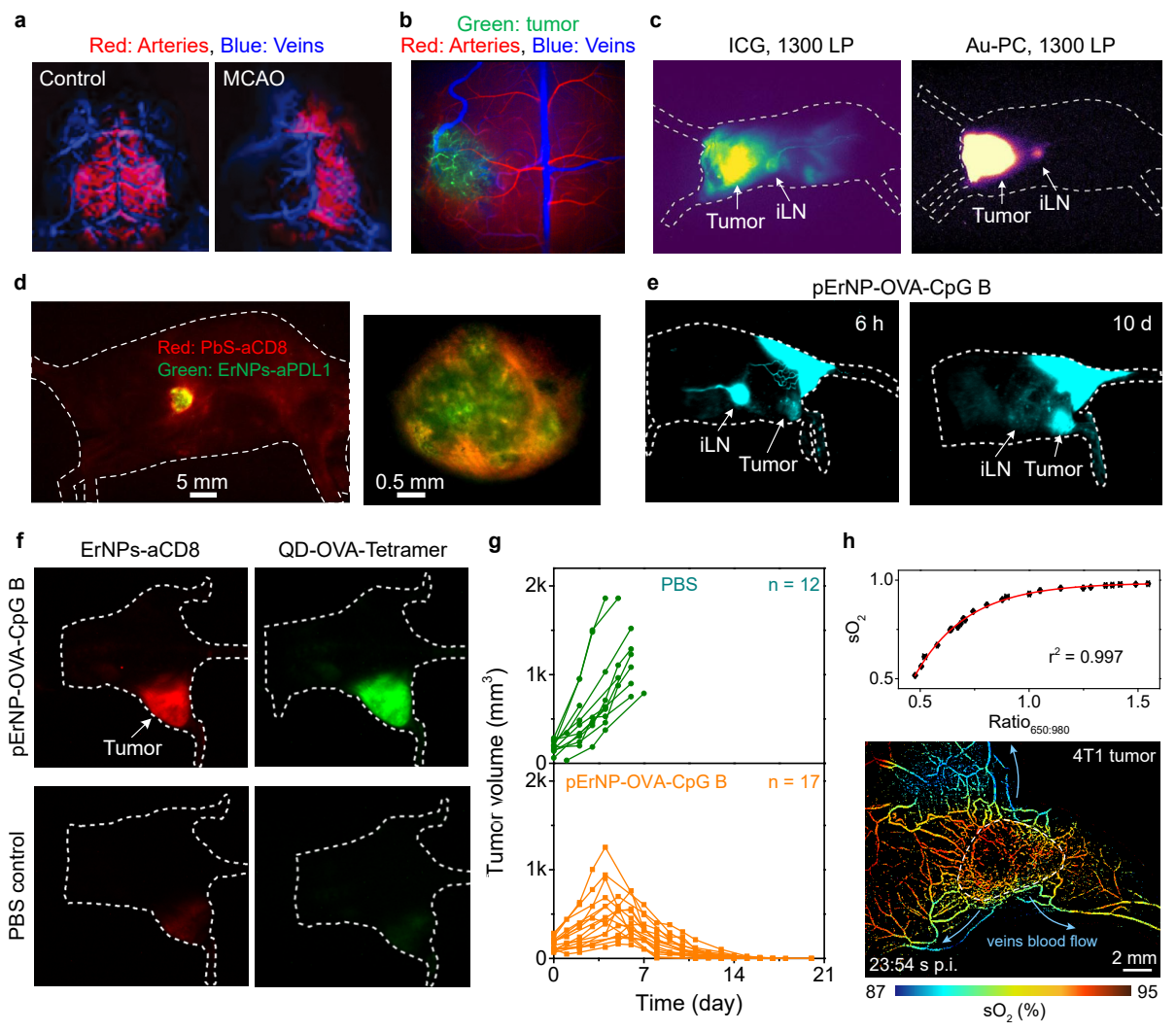
a
Red: Arteries, Blue: Veins
Control
MCAO
b
Green: tumor
Red: Arteries, Blue: Veins
c
ICG, 1300 LP
Au-PC, 1300 LP
Tumor
iLN
Tumor
iLN
d
Red: PbS-aCD8
Green: ErNPs-aPDL1
5 mm
0.5 mm
e
pErNP-OVA-CpG B
6 h
10 d
iLN
Tumor
iLN
Tumor
f
ErNPs-aCD8
QD-OVA-Tetramer
pErNP-OVA-CpG B
PBS control
Tumor
g
PBS
n = 12
pErNP-OVA-CpG B
n = 17
Tumor volume (mm3)
2k
1k
0
2k
1k
0
0
7
14
21
Time (day)
h
1.0
0.5
sO2
r2 = 0.997
0.5
1.0
1.5
Ratio650:980
4T1 tumor
veins blood flow
23:54 s p.i.
2 mm
87
95
sO2 (%)

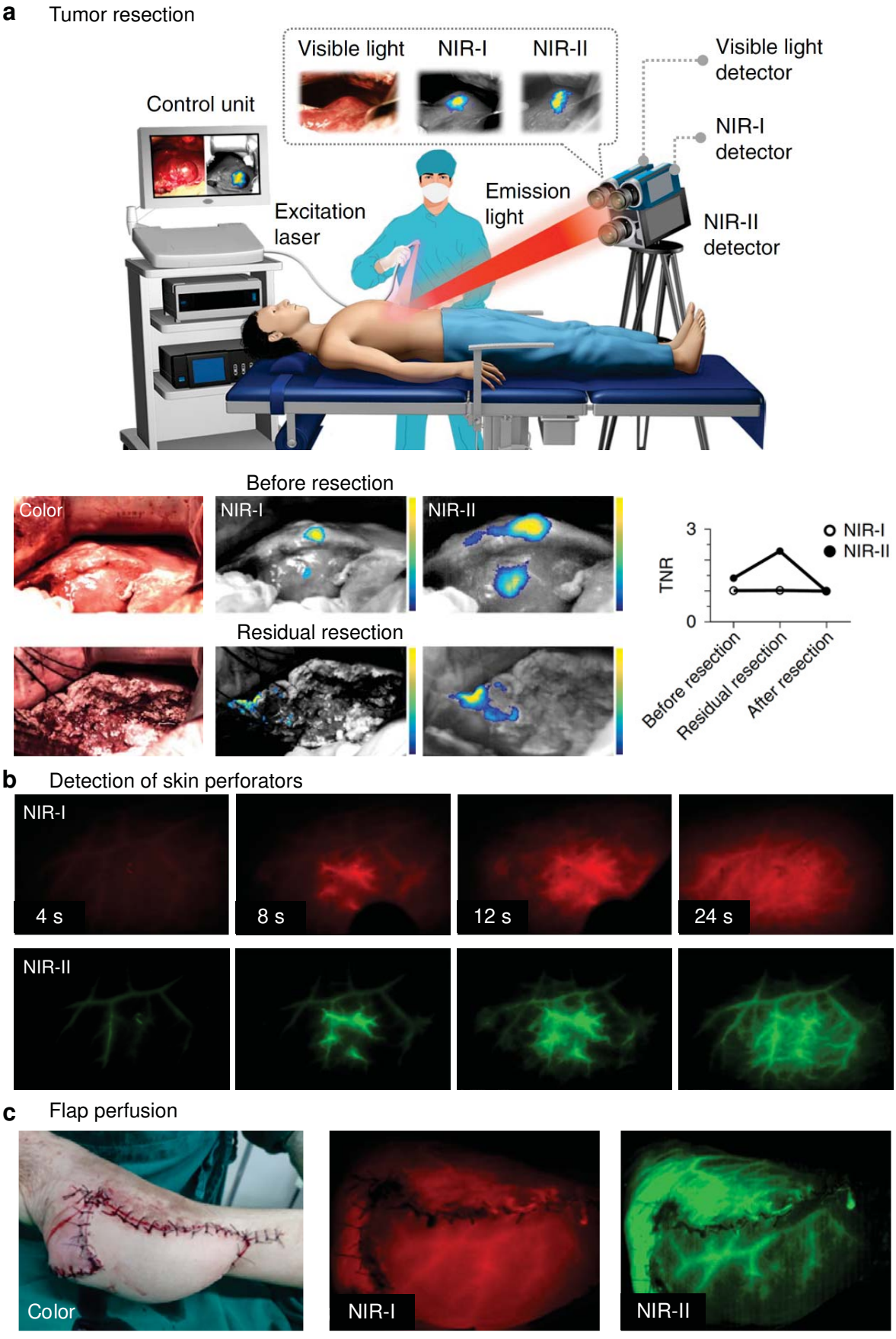
a
Tumor resection
Visible light
NIR-I
NIR-II
Visible light detector
NIR-I detector
NIR-II detector
Control unit
Excitation laser
Emission light
Before resection
Color
NIR-I
NIR-II
Residual resection
TNR
3
0
NIR-I
NIR-II
Before resection
Residual resection
After resection
b
Detection of skin perforators
NIR-I
4 s
8 s
12 s
24 s
NIR-II
c
Flap perfusion
Color
NIR-I
NIR-II